Development of an electrical impedance tomography set-up for the quantification of mineralization in biopolymer scaffolds

Development of an electrical impedance tomography set-up for the quantification of mineralization in biopolymer scaffolds

Marilisa Cortesi[1], Andrea Samoré[2], Joseph Lovecchio[3], Roberta Ramilli[4], Marco Tartagni[3], Emanuele Giordano[1,3,4]& Marco Crescentini[3,4]

[1] BioEngLab, Health Science and Technology, Interdepartmental Center for Industrial Research (HST-CIRI), Alma Mater Studiorum - University of Bologna, Ozzano Emilia, Italy;

[2] Department of Mathematics Alma Mater Studiorum - University of Bologna, Bologna, Italy;

[3] Laboratory of Cellular and Molecular Engineering "S.Cavalcanti", Department of Electrical, Electronic and Information Engineering "G.Marconi" (DEI), Alma Mater Studiorum − University of Bologna, Cesena, Italy;

[4] Advanced Research Center on Electronic Systems (ARCES), Alma Mater Studiorum, University of Bologna, Italy

E-mail: `marilisa.cortesi2@unibo.it`

Abstract. 3D cell cultures are becoming a fundamental resource for *in-vitro* studies, as they mimic more closely *in-vivo* behavior. The analysis of these constructs, however, generally rely on destructive techniques, that prevent the monitoring over time of the same construct, thus increasing the results variability and the resources needed for each experiment.

In this work, we focus on mineralization, a crucial process during maturation of artificial bone models, and propose electrical impedance tomography as an alternative non-destructive approach.

In particular, we discuss the development of an integrated hardware/software system capable of acquiring experimental data from 3D scaffolds and reconstructing the corresponding conductivity maps. We also show how the same software can test how the measurement is affected by biological features such as scaffold shrinking during the culture.

An initial validation, comprising the acquisition of both a non-conductive phantom and alginate/gelatin scaffolds with known calcium content will be presented, together with the *in-silico* study of a cell-induced mineralization process. This analysis will allow for an initial verification of the system's functionality while limiting the effects of biological variability due to cell number and activity.

Our results show the potential of electrical impedance tomography for the non-destructive quantification of matrix mineralization in 3D scaffolds, and open to the possible long term monitoring of this fundamental hallmark of osteogenic differentiation in hybrid tissue engineered constructs.

Quantification of mineralization through EIT   2

1. Introduction

Tissue engineering (TE) aims at developing artificial tissue substitutes with properties and characteristics equivalent to their natural counterpart: Barry et al. (2016), Hussey et al. (2018), Matta-Domjan et al. (2017). While mainly used to replace tissues damaged by injuries or diseases, these constructs have also become a valuable resource for *in-vitro* studies Pasini et al. (2021). Indeed, they are a more realistic model of *in-vivo* biology than traditional cell culture laboratory settings, and thus afford more accurate results when studying complex biological processes, the interaction between the cells and their environment and among different types of cells Inal et al. (2017), Ma et al. (2018).

The diffusion of these constructs as *in-vitro* models is however hampered by the lack of established and affordable techniques for their non-destructive characterization. Indeed the available approaches (micro-CT, micro-MRI, photoacoustic tomography) rely on complex, expensive instrumentation and occasionally require contrast-enhancing agents that could influence cellular processes and thus alter the measurement results Cai et al. (2013). Consequently, histological assays, which require the fixing and staining of the sample, have become a standard *de-facto* Calabrese et al. (2016), Picone et al. (2020). Since these methods result in the destruction of the sample, they effectively prevent the monitoring of the same construct throughout its development, increasing the time and the resources required for each experiment. Furthermore, variability among different scaffolds limits the accuracy of their characterization and the reproducibility of the results.

Recently, Electrical Impedance Tomography (EIT) has been proposed as a viable alternative for the non-destructive monitoring of 3D cell culture set-ups: Wu et al. (2018, 2019), De León et al. (2019), Lee et al. (2014), Yang et al. (2019), Canali et al. (2016). Indeed this technique is widely used for the imaging of internal structures of the human body, their monitoring over time, Shiraz et al. (2019), and the diagnosis of critical conditions Murphy et al. (2017), Samoré et al. (2017). The application of EIT to TE, however, is still underdeveloped and mainly focussed on the evaluation of cell viability Wu et al. (2018, 2019), Yang et al. (2019).

In this paper, we propose to apply the EIT technology to the quantification of the calcium content of polymeric scaffolds. To the best of our knowledge this is the first account of an integrated hardware/software system (HSS) developed to monitor this proxy for matrix mineralization, a property generally regarded as a fundamental feature for bone substitutes, strictly connected with the execution of osteogenesis and the mechanical properties of the construct Irie et al. (2008). In this respect, we here report a complete description of the proposed set-up, together with a preliminary experimental validation. In addition, the software platform integral to our HSS will be used to

Quantification of mineralization through EIT   3

simulate various stages of an osteogenic differentiation protocol and provide an initial evaluation of its effectiveness for the characterization of this complex biological process.

Comprehensively, the integrated HSS here described will be shown to be an effective framework for the development of novel tools helping TE development, providing researchers with an approach for the non-destructive characterization of mineralization in bone tissue substitutes.

2. Method

2.1. Description of the integrated hardware/software system

The HSS presented within this work combines an hardware set-up for the acquisition of voltage signals from a cylindrical measuring chamber featuring 8 electrodes and a software platform for the reconstruction of the conductivity maps from both experimental and simulated data.

A schematic representation of the acquisition setup is shown in Figure 1 (a). It includes an impedance analyser (Keysight E4990A), used both to generate the stimulus and record the output signal, a custom-made sample holder and a connection board. Eight electrodes have been inserted in holes (diameter: 1 mm) positioned at regular intervals on the side of the circular chamber at 2 mm of height from the bottom of the well (Figure 1(b)). The well of a 24-wells plate (internal diameter: 17 mm, internal height: 11 mm) was used as a model for this sample chamber, that was 3D-printed using Formlabs clear photopolymer resin. (Formlabs, Form 3).

The software component of the proposed HSS relies on Eidors (v3.9.1), a Matlab library featuring multiple algorithms for EIT forward and inverse problem solving. In particular, two common electrical models already available within Eidors (e2d3c and f2d3) were used as forward and inverse models respectively, to avoid the inverse crime. These are circular domains featuring 8 equidistant electrodes on the external perimeter and meshes with the number of triangular elements equal to 8463 and 7153.

The reconstruction algorithm presented in Adler & Guardo (1996) with a Tikhonov prior, was used throughout this analysis. This is an established approach for EIT reconstructions that is particularly effective for the retrieval of smooth conductivity distributions and the elimination of noise artifacts thanks to its regularization parameter, λ, that determines the level of smoothness.

The regions of the reconstructed maps associated with the objects of interest were isolated automatically through a segmentation procedure based on the Otsu's method (Figure 2). This algorithm relies on the histogram of the reconstructed conductivity map and identifies the threshold (th) associated with the maximal inter-cluster variance.

As the electrical properties of the solution filling the chamber (background) are not expected to change, the scaffold region (foreground) was then identified as the section of the histogram characterized by the highest conductivity variation (yellow overshadow in Figure 2).
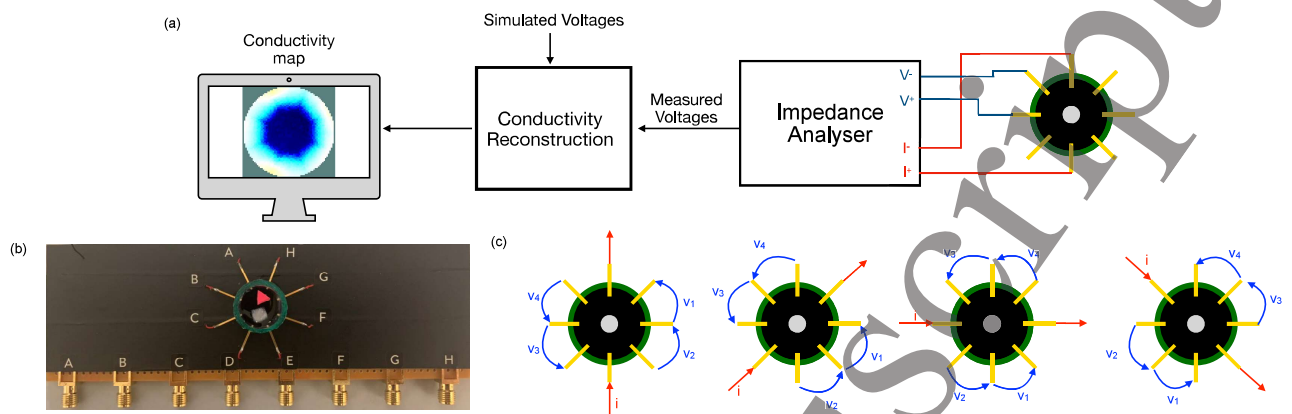
Quantification of mineralization through EIT

Figure 1. (a) The proposed HSS integrates (i) an impedance analyser (Keysight E4990A), (ii) a custom-made measurement chamber consisting of a cylindrical well fitted with 8 equidistant electrodes and (iii) a software system for reconstructing conductivity maps. The impedance analyser is used both to inject the current signal and to measure the resulting voltage, while the software system can be used with experimental or simulated voltages. (b) Picture of the custom measurement chamber. Each electrode is identified by a letter and linked to the corresponding cable connector. In this image the phantom (pink triangle) and one of the scaffolds (white circle) used within this work are visible. (c) Schematic representation of the opposite injection and adjacent measurement patterns for our 8-electrodes setup. Connections between the impedance analyser and the electrodes were manually changed but this step could be easily automated by using an electronic multiplexer.

2.2. Scaffold preparation

Alginate/gelatin scaffolds were prepared as follows. A 4% alginate solution and a 5% gelatin solution in distilled water were prepared and combined. Part of this mixture was supplemented with $CaCO_3$ (either 0.005 or 0.01 g/ml) and sonicated for about 20 minutes to reduce the size of the calcium aggregates. In this way, three different types of alginate/gelatin scaffolds are prepared which are intended to qualitatively represent the beginning, midpoint and conclusion of the osteogenic differentiation process. The wells of a 96 well plate were then filled with 300 μl of either calcium-supplemented ($CS_{0.005}, CS_{0.01}$) or calcium-free (CF) solutions and placed at 4° C for 30 minutes to allow for gelatin polymerization.

Successively the scaffolds were removed from the mould and each of them was placed in a solution of 400 mM $CaCl_2$ for 1 minute to allow for alginate polymerization. Scaffolds were then thoroughly washed with distilled water and maintained at 4° C in distilled water until their measurement.

2.3. Measurement protocol

A 4-electrode measurement technique was employed: the current stimulation was applied to opposite electrodes and the voltage was measured on adjacent electrodes as shown in
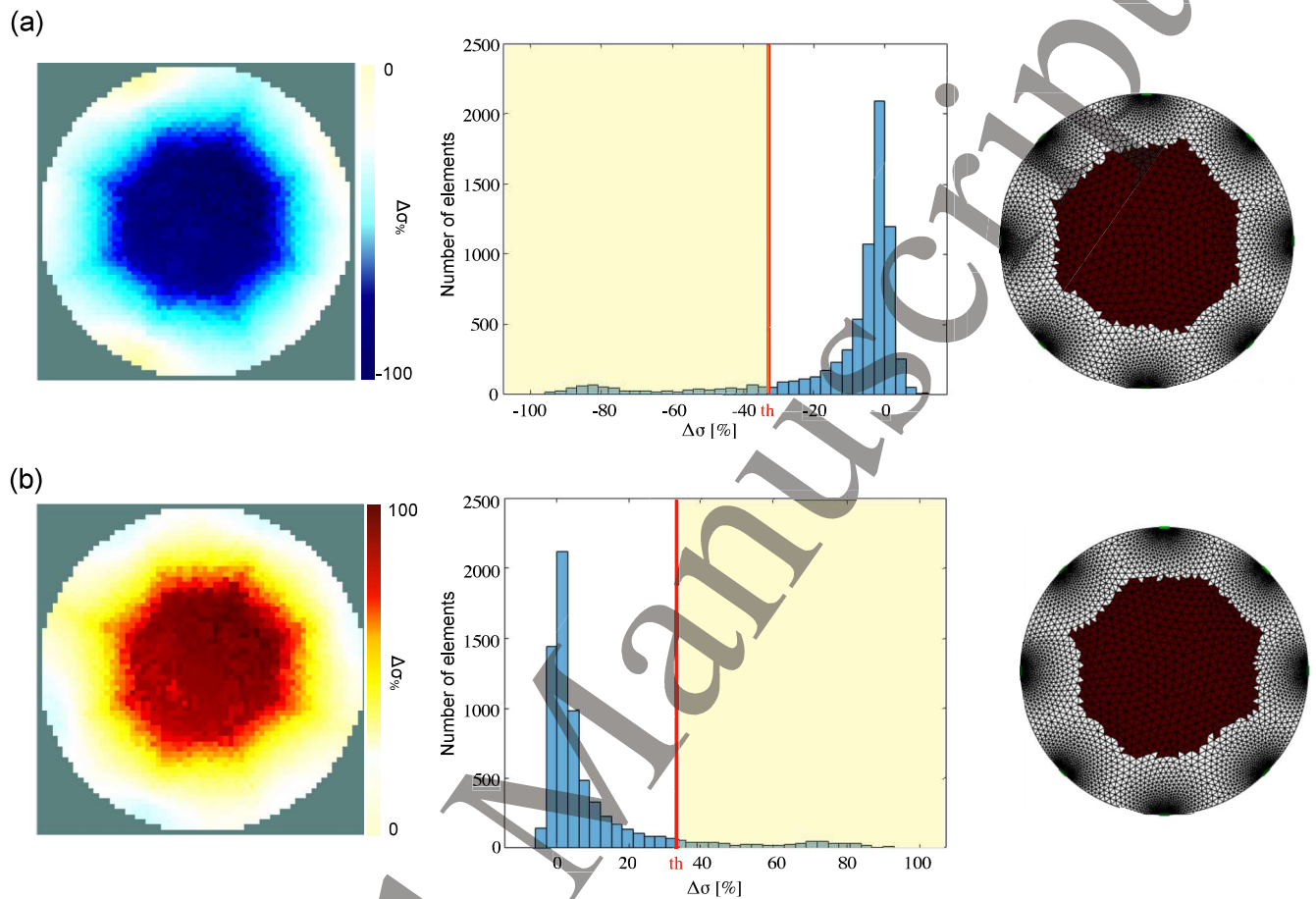
Figure 2. Segmentation algorithm used to automatically identify the elements of the mesh corresponding to the scaffold. The reconstructed conductivity maps (leftmost panels in (a) and (b)) are the input. Their histograms (central panels) are then analysed with the Otsu's algorithm that divides the mesh elements in two groups (threshold, th) so as to maximize inter-class variance. The scaffold elements are then identified as the ones associated with the highest $\Delta\sigma_{\%}$

Figure 1 (c). The voltage was sequentially measured on all the possible configurations of adjacent electrodes (since on defined as adjacent measurement layout). The procedure was replicated also for all the possible combinations of opposite electrodes to be used for current stimulation (since on defined as opposite stimulation pattern). The amplitude of the stimulation current was set to 200 μA and the frequency was linearly swept between 1 kHz and 40 kHz, a range commonly used for similar applications Samoré et al. (2017), Wu et al. (2018). The specific frequency used for the reconstructions was chosen through a specific parameter identification procedure described in the following sections (2.5 and 3.1). In all cases, both current and voltage were recorded. A total of 1 mL of 1 M HEPES buffer (σ=12.1 S/m, pH=7.4) filled the chamber during the measurements to create the conductive layer between the electrodes.

Quantification of mineralization through EIT   6

Table 1. Parameters estimated during the calibration procedure and their reference range.

Parameter	Value
λ	10^{-1}:10^{-15} step 10^{-1}
frequency	1 kHz to 40 kHz, 201 points linearly spaced

2.4. Parameters identification

The first step of the proposed analysis consists in the calibration of the reconstruction algorithm parameter (λ) and of the reconstruction frequency. In both cases, the data acquired using the synthetic rubber phantom were used and the reconstructed conductivity maps were normalized between 0 and 1 (Equation 1, where σ_R^{min} and σ_R^{max} are the minimum and maximum of the reconstructed conductivity variation).

$$\Delta\sigma_\% = \frac{\sigma_R - \sigma_R^{min}}{\sigma_R^{max}} \tag{1}$$

The average percentage conductivity variation ($\Delta\sigma_\%$ Equation 1) over all the mesh elements recognized as foreground (red elements in rightmost panels of Figure 2) was computed, for each considered parameter value (Table 1), and compared to its expected value ($\sigma_{T\%}$=-100%, Equation 2). The value of λ was then chosen as the one associated with the lowest difference from $\sigma_{T\%}$. As more than one value satisfied this condition, the smallest one was considered to avoid excessive filtering.

$$\sigma_{T\%} = 100 \cdot \frac{\sigma_E - \sigma_H}{\sigma_H} \tag{2}$$

Here, σ_E is the electrical conductivity of the synthetic rubber (1e-11 S/m) and σ_H that of the Hepes solution (12.1 S/m).

2.5. in-vitro analysis

Besides parameter estimation, the synthetic rubber phantom was also used to assess the spatial resolution uniformity of the system. To this end, measurements were acquired both with the object positioned at the center of the chamber and at its side, taking care to prevent contact between the phantom and the electrodes.

Successively, one CF and one CS scaffold, for each calcium levels, were considered. For this analysis, only the center position was evaluated, as scaffold positioning within the chamber can be directly controlled by the operator. For these samples, a time-difference reconstruction was considered, using the chamber filled with Hepes as baseline. This approach allowed us to quantify both the impedance of single scaffolds and the effects of the simulated mineralization.

Quantification of mineralization through EIT 7

2.6. in-silico simulations

The preliminary results obtained with the CSs and CF scaffolds were complemented by an extensive *in-silico* analysis aimed at assessing the feasibility of this method for the monitoring of mineralization within osteogenic differentiation.

To this end, the mineralization data obtained in Picone et al. (2020) with Alizarin Red were considered. The fraction of surface mineralization (M) retrieved over time (t) was fitted with a logistic curve (Equation 3) and the inferred values used to initialize the corresponding electrical model with a temporal resolution of 1 day (Supplementary Figure 1).

$$M = \frac{1}{1 + e^{-0.05 \cdot (t-200)}} \tag{3}$$

Coherently with the experimental set-up in Picone et al. (2020), the conductivity of the scaffold was set to 0.387 S/m Hasgall et al. (2018) while cell culture media (σ=1.4 S/m Chen et al. (2009)) was considered as background. Individual mesh elements, in a number equivalent to the corresponding fraction of mineralized surface, were set to the conductivity of cancellous bone (0.0829 S/m Hasgall et al. (2018)). To realistically model the biological process, the same electrical model was maintained throughout the analysis and only incremental changes in mineral fraction were added. Noteworthy, 3D scaffolds have been noticed to shrink throughout osteogenic differentiation James-Bhasin et al. (2018), possibly due to the reorganization of collagen fibers. This effect is quite complex to characterize experimentally, due to the technical difficulty in building suitable phantoms and isolating this variable from other relevant quantities, but , is particularly relevant for the analysis here described as the change in object to vessel ratio influences the current path within the chamber and hence the result. To fully model this effect, a linear decrease in size was hypothesized and multiple percentage decrease endpoints (10%:70% with 10% steps) were considered.

To evaluate this aspect, while maintaining complete control over scaffold composition, the software platform integral to our HSS will be used to simulate various stages of an osteogenic differentiation protocol and provide an initial evaluation of its effectiveness for the characterization of this complex biological process.

This analysis relied on the same reconstruction algorithm and parameters detailed in the previous section and all the simulations included the addition of noise to the voltage data prior to the reconstruction (SNR=50 dB). The only difference was the approach used to isolate the mesh elements corresponding to the scaffold. Since they were known a priori, the segmentation procedure was not applied and the region of interest was directly inferred from the electrical model (Supplementary Figure 2).
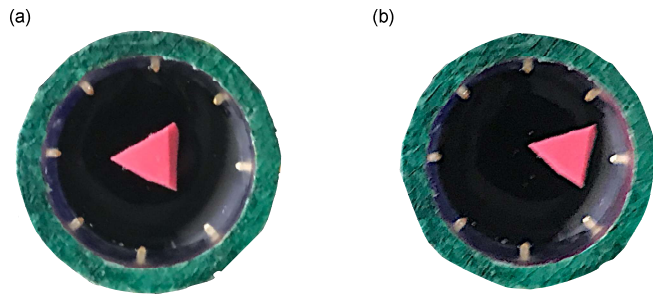
Quantification of mineralization through EIT   8

Figure 3. Images of the synthetic rubber phantom positioned either at the center (a) or the side (b) of the measurement chamber

3. Results

3.1. System calibration and parameters setup

The initial tests with the proposed system involved the reconstruction of the conductivity map of the set-up in Figure 3 (a), where the synthetic rubber phantom (pink triangle) was positioned at the center of the measurement chamber filled with Hepes solution.

These measures were used to set the parameter of the reconstruction algorithm (λ) that determines the level of smoothness of the reconstruction. The identification of this parameter is key for obtaining an accurate conductivity map, as a value too large will filter out some of the signal, while one too little will yield a solution contaminated by propagated error Park et al. (2018). While several methods are available for the identification of λ Bauer & Hohage (2005), Hämarik & Raus (2009), Hansen & O'Leary (1993), Tikhonov & Glasko (1965), no approach has been shown to be consistently better than the others Benvenuto & Jin (2020). As choosing the wrong strategy, and hence the wrong λ, can compromise significantly the accuracy of the reconstruction we decided to compute 15 different reconstructions, each corresponding to a different parameter value (10^{-1}: 10^{-15} step 10^{-1}), and to compare the reconstructed conductivity variation (Figure 4 (a)) to its expected value (Equation 2).

Values above 10^{-5} were determined to be associated with the lowest average error (LAE=34%, computed as in Equation 4). As such λ was set to 10^{-5} to ensure a low error while avoiding excessive smoothing of the reconstructed data.

$$LAE = \frac{|\sigma_{T\%} - \Delta_{\sigma\%}|}{|\sigma_{T\%}|} \tag{4}$$

Successively the reconstructed conductivity variation corresponding to each available frequency was computed (Figure 4 (b)). A negligible dependency of the results on the stimulation frequency, within the considered range, was ascertained. Consequently, the frequency of 19.3 kHz, corresponding to the middle of the available range, was considered for the remainder of the analysis.
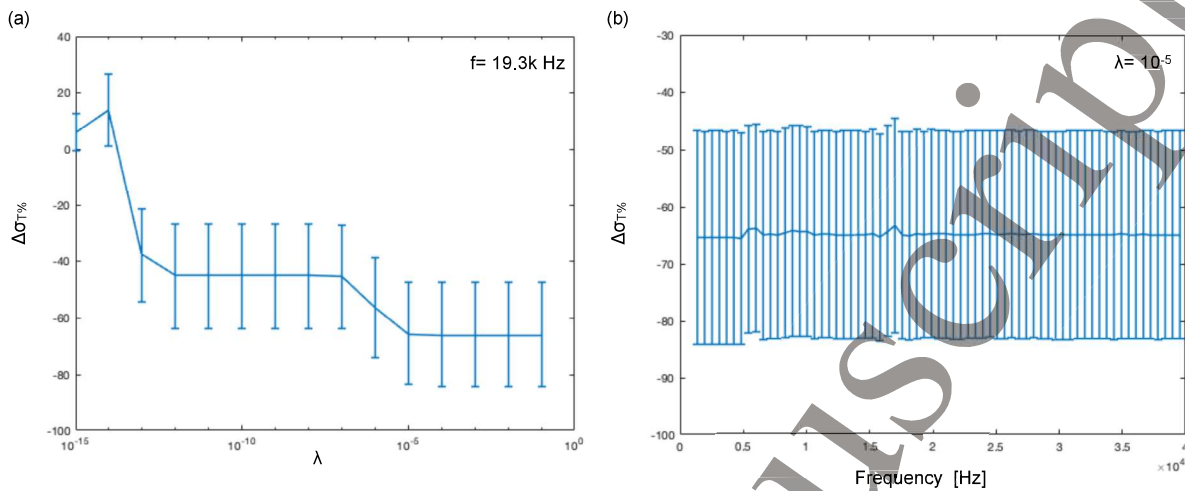
Figure 4. Parameters identification. (a) Average difference in the conductivity percentage change as a function of the reconstruction algorithm parameter (λ). Bars represent the standard deviation of $\Delta\sigma_{T\%}$ within the scaffold region. (b) Representation of the dependence of the error in reconstructed conductivity change as a function of frequency. Bars represent the standard deviation of $\Delta\sigma_{T\%}$ within the scaffold region. For graphical clarity, only 2/3 of the available data points are reported.

Reconstructing the conductivity of the two configurations in Figure 3 results in the maps reported in Figure 5 (a) and (d). The different phantom position within the chamber is correctly identified and a slightly triangular shape is recovered for the side positioning. This is also confirmed by the output of the segmentation procedure (Figures 5 (c) and (f)) that shows how the proposed method effectively recognizes the region of interest.

The conductivity profiles (Figure 5 (b), (e)) at the center of the chamber (red line in Figure 5 (a)) and at 2/3 of its diameter (red line in Figure 5 (d)) highlight a slightly non-uniform internal conductivity and a difference between the reconstructed conductivity variation and the ground truth of about 15%.

3.2. Experimental measurement of polymeric scaffolds for TE applications

The proposed HSS was used to reconstruct the conductivity map of alginate/gelatin scaffolds polymerized with ($CS_{0.05}$, $CS_{0.1}$) or without (CF) $CaCO_3$. These were developed to mimic a mineralization process occurring in a polymeric scaffold during osteogenic differentiation, while maintaining a strict control over sample composition and preserving its uniformity. Indeed osteogenesis results in bone extracellular matrix mineralization leading to the synthesis of hydroxyapatite, a calcium phosphate compound Picone et al. (2020). As cell status and distribution can affect the results, we preferred to use un-cellularized scaffolds supplemented with controlled levels of $CaCO_3$ to ensure more accurate testing of the proposed system. This choice, in addition, removes from the analysis any error due to the quantification of Alizarin red staining,
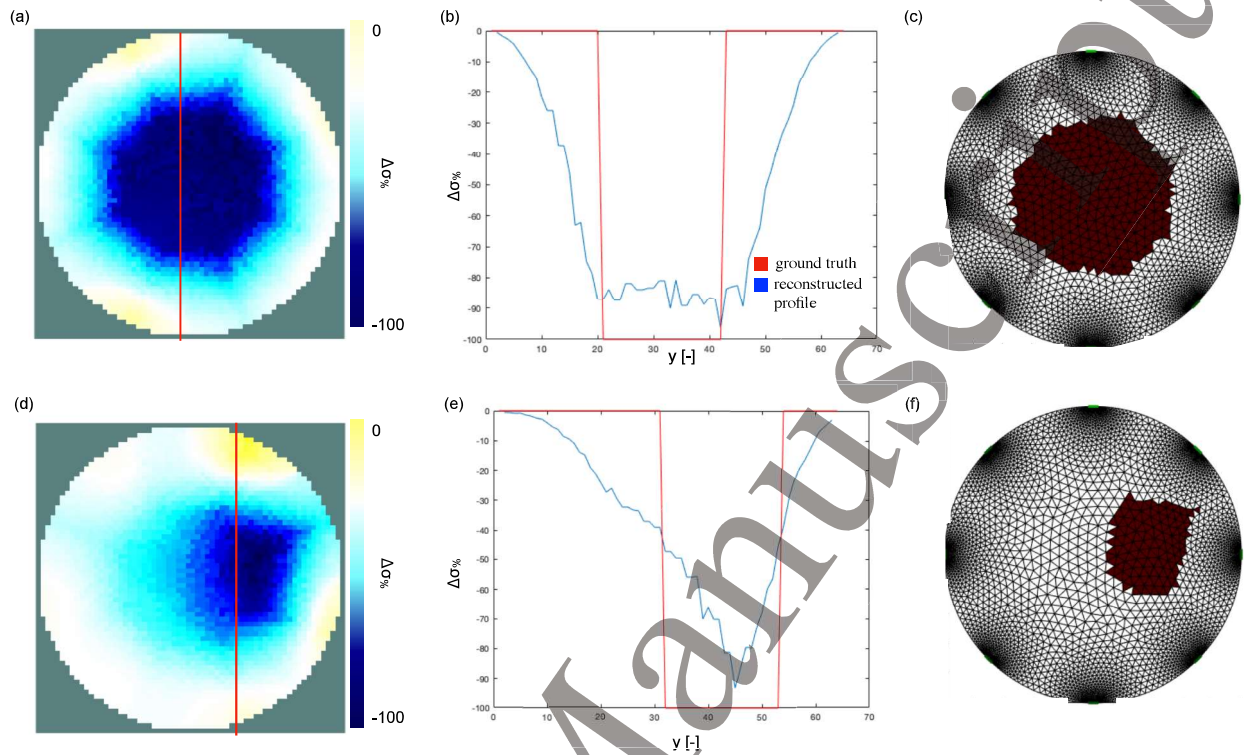
Figure 5. Conductivity reconstruction of the synthetic rubber phantom positioned in two different regions of the measurement chamber (center and side). (a) and (d) show the conductivity maps of the center and side conditions respectively. (b) and (e) outline the profiles of the reconstructed regions and the corresponding ground truth, while (c) and (f) show the segmented regions.

which can be non-negligible Eggerschwiler et al. (2019) and can be influenced by the specific section considered. Figure 6 shows the results of this analysis.

All scaffolds result in a decrease in conductivity, when compared to the Hepes solution. The intensity of this variation, however, is proportional to the scaffold's calcium content (Figure 6(b) and (c)). In particular the addition of the CF scaffold results in an almost null conductivity variation, while the addition of 0.1 g/ml of $CaCO_3$ induces a decrease in $\Delta\sigma$ that is almost twice that registered when considering $CS_{0.05}$. In all cases, reconstructed scaffolds are characterized by a fairly uniform conductivity.

3.3. in-silico analysis of cell-induced mineralization

While providing an initial verification of the effectiveness of our HSS, the *in-vitro* characterization presented in the previous sections is not sufficient to demonstrate the usefulness of the proposed set-up for the quantification of mineralization within an osteogenic protocol. Indeed, the total increase in calcium content due to cell activity might differ from the ones considered in this work (0.05, 0.1 g/ml) and three different calcium levels are a rather simplified representation of cell-induced mineralization.

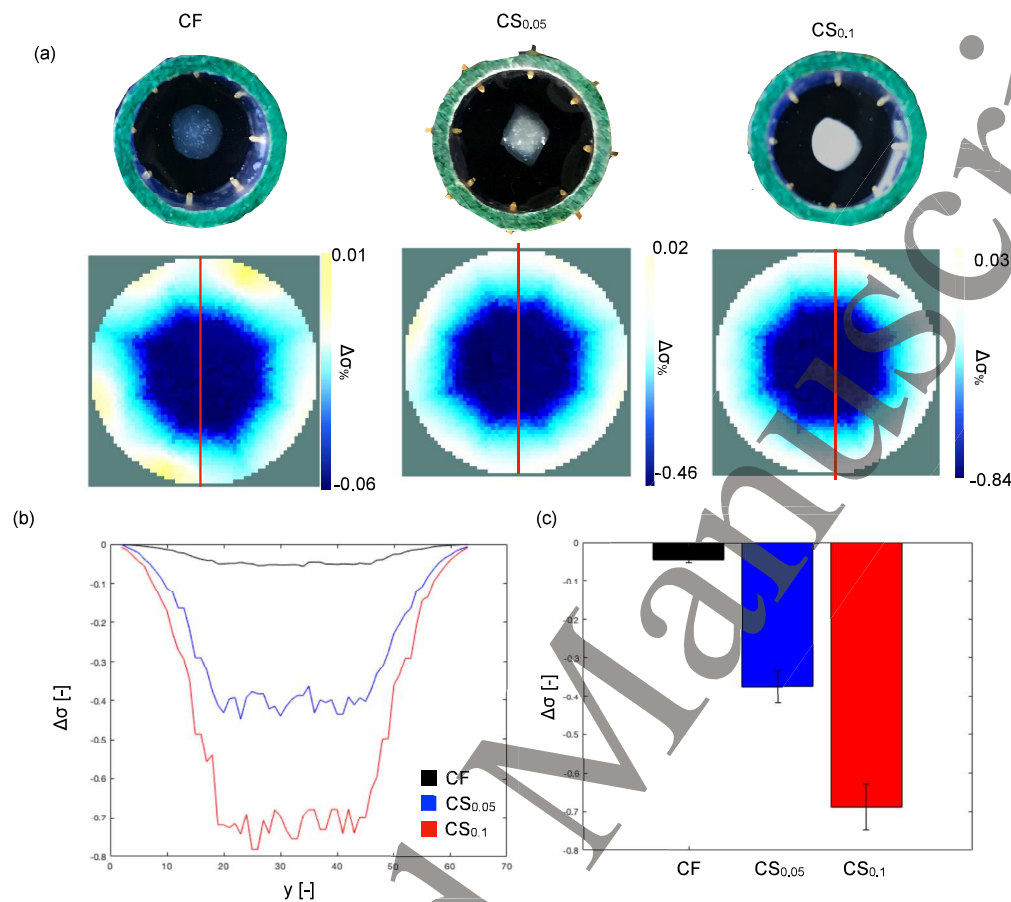As such, the experimental study presented in the previous sections was

Figure 6. (a) Pictures and conductivity reconstructions of the CF and CSs scaffolds, considering the chamber containing Hepes solution as background. (b) Reconstructed conductivity profiles at the center of the chamber (red lines in the conductivity maps) for all considered conditions and (c) average ($+$/- standard deviation) conductivity within the segmented region

complemented by an *in-silico* analysis aimed at replicating the acquisition of voltage signals from samples undergoing an osteogenic differentiation process. To improve the accuracy of this study, the percentage of mineralized surface experimentally measured in Picone et al. (2020) at different time points during osteogenic differentiation was considered. A logistic function (Equation 3) was used to fit the experimental data thus allowing to infer the mineralization level at any point throughout the experiment (Supplementary Figure 1). These results were used to build electrical models representing the status of the scaffold throughout a 14 days mineralization process. The conductivity distributions were then reconstructed, following the addition of noise (SNR=50 dB), using the same algorithm and parameters previously detailed.

Figure 7 shows the results of this analysis. In (a) the average variation in conductivity in the scaffold region is reported. As for the CSs and CF scaffolds, an
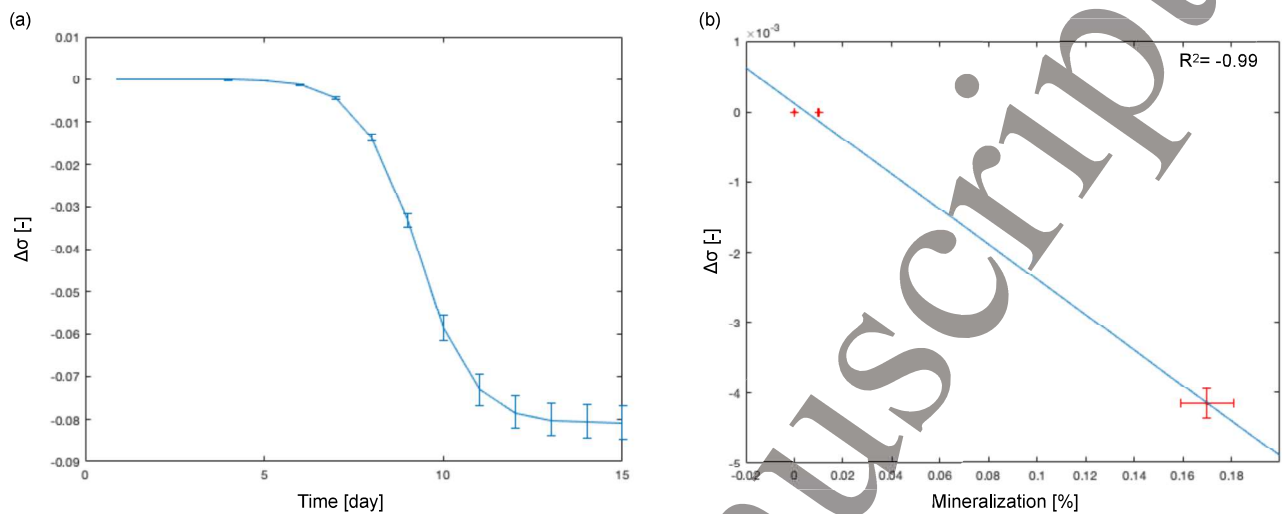
Figure 7. Simulation of the mineralization associated with osteogenic differentiation. (a) Percentage variation in conductivity in the region recognized as part of the scaffold. (b) Correlation between the percentage of the mineralized area measured inPicone et al. (2020) and the average reconstructed conductivity variation at the same time point.

increase in mineralization corresponds to a decrease in conductivity. This becomes apparent about seven days after the beginning of the experiment (corresponding to a mineralization of about 15%) and closely matches the experimental results obtained with Alizarin red (Figure 7 (b)). Indeed the Pearson's correlation coefficient between the simulated and *in-vitro* data is -0.99.

Another characteristic of osteogenic differentiation in polymeric scaffolds is their shrinking, which is often connected with the cells' ability to modify their surrounding matrix James-Bhasin et al. (2018). To study the effect of this phenomenon on the reconstructed conductivity distribution, 7 different percentage reductions in surface area were considered (10, 20, 30, 40, 50, 60, 70 %). A linear relationship (Figure 8(a)) was used to model this process, which was assumed to occur over a period of 14 days. Both the time scale and the amplitude of this phenomenon are coherent with the experimental results James-Bhasin et al. (2018).

The average reconstructed conductivity variations within the scaffold are shown in Figure 8(b). Limited changes in scaffold size ($<30\%$) result in conductivity profiles substantially equivalent to the one shown in Figure 7, where the size of the scaffold was not modified. On the other hand, important changes in object size ($> 40\%$), exhibit the opposite behaviour, with a conductivity increment over time. This is coherent with a mismatch between the rate at which the two processes (i.e. mineralization and shrinking) are occurring. Indeed a rapid increase in the fraction of the chamber occupied by cell culture media, the most conductive material in our set-up, effectively masks the change in scaffold composition, resulting in a net increase in $\Delta\sigma$. This is particularly prominent at the beginning and end of the time course, where the matrix composition
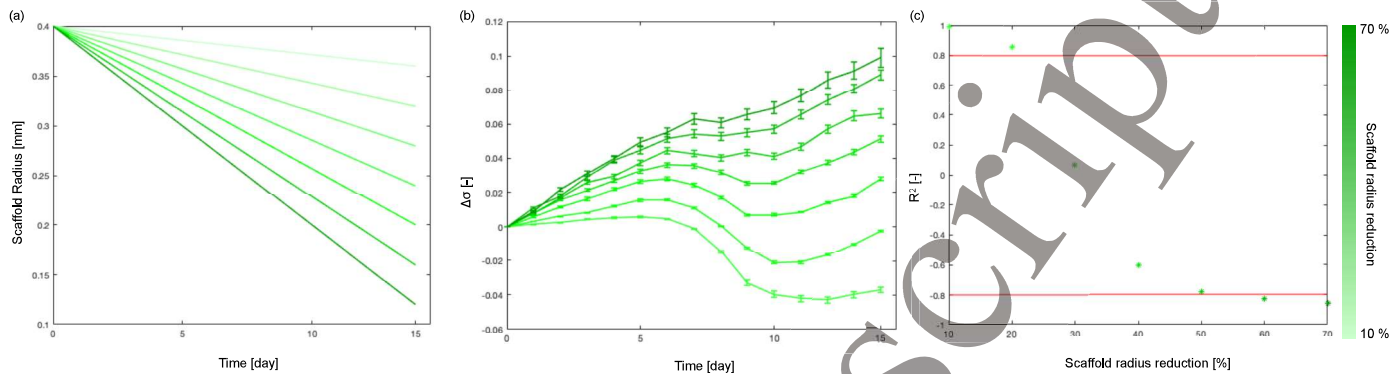
Figure 8. Simulation of the mineralization associated with osteogenic differentiation taking into account the reduction in scaffold size. (a) Linear equations describing scaffold radius reduction over time. (b) Corresponding percentage variation in reconstructed conductivity. (c) Pearson's correlation coefficient between the actual and reconstructed scaffold conductivity for each considered percentage reduction in scaffold size. Red lines identify a correlation equal to +/- 80%.

is approximately constant (Figure 7 (a)), and less evident between day 7 and 10, where the rate of change in mineralization-induced conductivity is higher.

In all cases a strong correlation with the actual scaffold conductivity is maintained (Figure 8(c)). Indeed both small ($< 30\%$) and large ($> 40\%$) scaffold area reductions have a Pearson's correlation coefficient of at least 80%, when compared to the actual average scaffold conductivity.

While experimental confirmation will be needed to definitely validate the proposed system as a viable approach for non-invasive mineralization monitoring during osteogenic differentiation, these results clearly show the potential of this approach as an alternative to destructive assays such as Alizarin based histology.

4. Discussion

In this paper, we have described a HSS integrating hardware and software components for the non-destructive quantification of mineral content in polymeric scaffolds and the study of complex biological behaviours in a controlled environment. Both the application to TEed constructs and the synergy between *in-vitro* and *in-silico* results are key innovations of this method, that we propose as an alternative to histological analysis or other expensive techniques for the evaluation of osteogenic differentiation. Indeed, while we have presented the use of an impedance analyzer (Keysight E4990A) for both the generation of the current stimulus and the measurement of the voltage signal, this instrument could be effectively substituted with systems realized *ad-hoc* such as the prototypes reported in Luciani et al. (2019) and Tan et al. (2020) or commercial devices like the AD5933 or the AD5940 from Analog Devices, allowing for a significant cost reduction.

We have demonstrated the ability of this system to quantify the variations in

conductivity distribution induced both by a non-conductive object (synthetic rubber phantom) and by alginate/gelatin scaffolds polymerized in absence or presence of a defined amounts of calcium. These experimental results show the feasibility of EIT as a useful technique for the non-destructive characterization of TEed constructs.

Additionally, an extensive *in-silico* analysis has been conducted to reproduce a cell-induced mineralization process. Experimental data from the recent scientific literature have been extensively used to set-up the simulations and test the effectiveness of the reconstruction algorithm within the considered application. In particular, the effect of reducing the scaffold size throughout the osteogenic differentiation protocol has been evaluated. This is a commonly observed consequence of osteogenic differentiation connected with the cells' ability to remodel their collagen environment and depose new extracellular matrix. Our results showed an inversion in the direction of conductivity change, upon reducing the scaffold area of more than 40% over 14 days. This is likely connected with the comparatively small change in average scaffold conductivity, with respect to the rate of scaffold shrinkage. The average conductivity variation within the scaffold, however, maintained a high correlation with the actual value in most of the tested conditions.

While representing an important proof-of-concept, the proposed set-up has a number of limitations. Among them, the low number of electrodes results in poor spatial resolution and inaccurately reconstructed shapes. Having direct access to the scaffold, its shape and positioning, partially mitigates this issue, that is expected to be addressed by an automatic electrodes switching mechanism, currently under development in our laboratory. This upgrade will also drastically reduce the time needed for the acquisition of each sample, allowing for a more extensive experimental validation including cellularized scaffolds and osteogenic differentiation protocols.

A key element of our set-up that will be further developed in the future is the integration between hardware and software. Indeed, computational models have been shown to be able to effectively predict the results of *in-vitro* experiments Cortesi et al. (2019, 2020*a*,*b*, 2021), Passini et al. (2017), providing an environment for hypotheses testing and experimental conditions optimization. Within this context, the combination of experimental measurements and *in-silico* methods could allow for the real-time prediction of each construct's mineralization dynamic and for the adjustment of the osteogenic induction stimulus and culture conditions to each specific scaffold.

This feature, while not showcased in the results of this work, due to the static mineralization level of the considered samples, would only require small adjustments to the presented system (i.e. use of a bioreactor system and implementation of its control software). A similar approach has been pioneered in de Bournonville et al. (2019) where media replacement was adapted to the actual nutrients level in the culture. The approach here proposed could go one step further, exploiting the results of the *in-silico* analysis to optimize the osteogenic differentiation protocol and thus improve its reproducibility in highly complex, potentially heterogeneous setups.

As such we believe the system here described to be an important innovation in TE,

REFERENCES   15

providing an affordable, non-invasive approach for the quantification of mineralization in polymeric scaffolds. Another unique feature of our setup, which sets it apart from the most common applications of EIT, is the complete knowledge of the measurement chamber layout and of the scaffold position. This opens to the possibility of integrating additional knowledge within the reconstruction algorithm using an approach such as the one described in Huska et al. (2020). This modification is expected to further improve the reconstruction accuracy and possibly highlight intra-scaffold non-uniformities in mineralization spatial distribution, a key element in the pre-implant characterization of bone tissue substitutes.

Moreover, a change in measurement frequency could make this technique capable of estimating functional characteristics, such as cell viability Wu et al. (2018) and distribution within the scaffold. The possibility of quantifying multiple variables on the same sample and follow their evolution over time would constitute a fundamental advancement for TE and the development of both artificial tissue substitutes and 3D cell culture models.

Finally, the small size of the device would allow for effective integration within continuous culture devices that allow for more physiological culture conditions Ciardulli et al. (2020), Govoni et al. (2016), Lovecchio et al. (2014), Lovecchio, Pannella, Giardino, Calzá & Giordano (2019), Pasini et al. (2017) and have been demonstrated to effectively induce osteogenic commitment in stem cells Lovecchio, Gargiulo, Vargas Luna, Giordano & Sigurjónsson (2019). This versatility is an important characteristic of this method that could determine its success in the field and promote its advancement in a sustainable and cost-effective way.

Conflict of Interest

The authors declare no conflict of interest

Acknowledgment

References

Adler, A. & Guardo, R. (1996), 'Electrical impedance tomography: regularized imaging and contrast detection', *IEEE Transactions on Medical Imaging* .

REFERENCES

https://doi.org/10.1109/42.491418.

Barry, M., Pearce, H., Cross, L., Tatullo, M. & Gaharwar, A. (2016), 'Advances in nanotechnology for the treatment of osteoporosis', *Current Osteoporosis Reports* . https://doi.org/10.1007/s11914-016-0306-3.

Bauer, F. & Hohage, T. (2005), 'A lepskij-type stopping rule for regularized newton methods', *Inverse Problems* . http://dx.doi.org/10.1088/0266-5611/21/6/011.

Benvenuto, F. & Jin, B. (2020), 'A parameter choice rule for tikhonov regularization based on predictive risk', *Inverse Problems* . https://doi.org/10.1088/1361-6420/ab6d58.

Cai, X., Zhang, Y., Xia, Y. & Wang, L. (2013), 'Photoacoustic microscopy in tissue engineering', *Materials Today* . https://doi.org/10.1016/j.mattod.2013.03.007.

Calabrese, G., Giuffrida, R., Fabbri, C., Figallo, E., Lo Furno, D., Gulino, R., Colarossi, C., Fullone, F., Giuffrida, R., Parenti, R., Memeo, L. & Forte, S. (2016), 'Collagen-hydroxyapatite scaffolds induce human adipose derived stem cells osteogenic differentiation *in vitro*', *PLOS ONE* . https://doi.org/10.1371/journal.pone.0151181.

Canali, C., Aristovich, K., Ceccarelli, L., Larsen, L., Martinsen, O. G., Wolff, A., Dufra, M., Emnéus, J. & Heiskanen, A. (2016), 'Electrical impedance tomography methods for miniaturised 3d systems', *Journal of Electrical Bioimpedance* . https://doi.org/10.5617/jeb.4084.

Chen, M., Jiang, C., Vernier, P., Wu, Y. & Gundersen, M. (2009), 'Two-dimensional nanosecond electric field mapping based on cell electropermeabilization', *PMC Biophysics* . https://doi.org/10.1186/1757-5036-2-9.

Ciardulli, M., Marino, L., Lovecchio, J., Giordano, E., Forsyth, N., Selleri, C., Maffulli, N. & Della Porta, G. (2020), 'Tendon and cytokine marker expression by human bone marrow mesenchymal stem cells in a hyaluronate/poly-lactic-co-glycolic acid (plga)/fibrin three-dimensional (3d) scaffold.', *Cells* . https://doi.org/10.3390/cells9051268.

Cortesi, M., Liverani, C., Mercatali, L., Ibrahim, T. & Giordano, E. (2020*a*), 'Computational models to explore the complexity of the epithelial to mesenchymal transition in cancer.', *WIREs Systems Biology and Medicine* . https://doi.org/10.1002/wsbm.1488.

Cortesi, M., Liverani, C., Mercatali, L., Ibrahim, T. & Giordano, E. (2020*b*), 'An in-silico study of cancer cell survival and spatial distribution within a 3d microenvironment.', *Scientific Reports* . https://doi.org/10.1038/s41598-020-69862-7.

Cortesi, M., Liverani, C., Mercatali, L., Ibrahim, T. & Giordano, E. (2021), 'Development and validation of an in-silico tool for the study of therapeutic agents in 3d cell cultures', *Computers in Biology and Medicine* . https://doi.org/10.1016/j.compbiomed.2021.104211.

Cortesi, M., Pasini, A., Furini, S. & Giordano, E. (2019), 'Identification via numerical computation of transcriptional determinants of a cell phenotype decision making.', *Frontiers in Genetics* . https://doi.org/10.3389/fgene.2019.00575.

REFERENCES

de Bournonville, S., Lambrechts, T., Vanhulst, J., Luyten, F., Papantonniou, I. & Geris, L. (2019), 'Towards self-regulated bioprocessing: a compact benchtop bioreactor system for monitored and controlled 3d cell and tissue culture.', *Biotechnology Journal* . https://doi.org/10.1002/biot.201800545.

De León, S., Popuvac, A. & SL, M. (2019), 'Three-dimensional (3d) cell culture monitoring: Opportunities and challenges for impedance spectroscopy', *Biotechnology and Bioengineering* . https://doi.org/10.1002/bit.27270.

Eggerschwiler, B., Canepa, D. D., C, P. H., A, C. E. & Cinelli, P. (2019), 'Automated digital image quantification of histological staining for the analysis of the trilineage differentiation potential of mesenchymal stem cells', *Stem Cell Research & Therapy* . https://doi.org/10.1186/s13287-019-1170-8.

Govoni, M., Muscari, C., Lovecchio, J., Guarnieri, C. & Giordano, E. (2016), 'Mechanical actuation systems for the phenotype commitment of stem cell-based tendon and ligament tissue substitutes.', *Stem Cell Reviews and Reports* . https://doi.org/10.1007/s12015-015-9640-6.

Hämarik, U. & Raus, T. (2009), 'About the balancing principle for choice of the regularization parameter', *Numerical Functional Analysis and Optimization* . https://doi.org/10.1080/01630560903393139.

Hansen, P. C. & O'Leary, D. P. (1993), 'The use of the l-curve in the regularization of discrete ill-posed problems', *SIAM Journal on Scientific Computing* . https://doi.org/10.1137/0914086.

Hasgall, P., Di Gennaro, F., Baumgartner, C., Neufeld, E., Lloyd, B., Gosselin, M., Payne, D., A., K. & Kuster, N. (2018), 'It'is database for thermal and electromagnetic parameters of biological tissues.', - . Version 4.0, May 15, 2018.

Huska, M., Lazzaro, D., Morigi, S., Samoré, A. & Scrivanti, G. (2020), 'Spatially-adaptive variational reconstructions for linear inverse electrical impedance tomography.', *Journal of Scientific Computing* . https://doi.org/10.1007/s10915-020-01295-w.

Hussey, G. S., Dziki, J. & Badylak, S. F. (2018), 'Extracellular matrix-based materials for regenerative medicine.', *Nature Reviews Materials* . https://doi.org/10.1038/s41578-018-0023-x.

Inal, S., Hama, A., Ferro, M. ands Pitsalidis, C., Oziat, J., Iandolo, D., Pappa, A., Hadida, M., Huerta, M., Marchat, D., Mailley, P. & Owens, R. (2017), 'Conducting polymer scaffolds for hosting and monitoring 3d cell culture.', *Advanced Biosystems* . https://doi.org/10.1002/adbi.201700052.

Irie, K., Ejiri, S., Sakakura, Y., Shibui, T. & Yajima, T. (2008), 'Matrix mineralization as a trigger for osteocyte maturation.', *Journal of Histochemistry and Cytochemistry* . https://doi.org/10.1369/jhc.2008.950527.

James-Bhasin, M., Siegel, P. & Nazhat, S. (2018), 'A three-dimensional dense

REFERENCES

collagen hydrogel to model cancer cell/osteoblast interactions.', *Journal of Functional Biomaterials* . https://doi.org/10.3390/jfb9040072.

Lee, E., McEwan, A., Farooq, A., Sohal, H., Woo, E., Seo, J. & Oh, T. (2014), 'Design of a microscopic electrical impedance tomography system for 3d continuous non-destructive monitoring of tissue culture', *BioMedical Engineering OnLine* . https://doi.org/10.1186/1475-925X-13-142.

Lovecchio, J., Gargiulo, P., Vargas Luna, J., Giordano, E. & Sigurjónsson, O. (2019), 'A standalone bioreactor system to deliver compressive load under perfusion flow to hbmsc-seeded 3d chitosan-graphene templates.', *Scientific Reports* . https://doi.org/10.1038/s41598-019-53319-7.

Lovecchio, J., Jonsdottir-Buch, S., Einarsdottir, G., Gislason, M., Orlygsson, G., Gargiulo, P. & Sigurjonsson, O. (2014), 'Assessment of a perfusion bioreactors system using μct technology and 3d modeling methods.', *BIOMEDIZINISCHE TECHNIK* . https://doi.org/10.1515/bmt-2014-5003.

Lovecchio, J., Pannella, M., Giardino, L., Calzá, L. & Giordano, E. (2019), 'A dynamic culture platform enhances the efficiency of the 3d huvec-based tube formation assay.', *Biotechnology and Bioengineering* . https://doi.org/10.1002/bit.27227.

Luciani, G., Ramilli, R., Romani, A., Tartagni, M., Traverso, P. & Crescentini, M. (2019), 'A miniaturized low-power vector impedance analyser for accurate multi-parameter measurement', *Measurement* **144**, 388–401.

Ma, X., Liu, J., Zhu, W., Tang, M., Lawrence, N., Yu, C., M., G. & Chen, S. (2018), '3d bioprinting of functional tissue models for personalized drug screening and in vitro disease modeling.', *Advanced Drug Delivery Reviews* . https://doi.org/10.1016/j.addr.2018.06.011.

Matta-Domjan, B., King, A., Totti, S., Matta, C., Dover, G., Martinez, P., Zakhidov, A., La Ragione, R., Macedo, H., Jurewicz, I., Dalton, A. & Velliou, E. (2017), 'Biophysical interactions between pancreatic cancer cells and pristine carbon nanotube substrates: potential application for pancreatic cancer tissue engineering.', *Journal of Biomedical Materials Research, Part B* . https://doi.org/10.1002/jbm.b.34012.

Murphy, E., Mahara, A., Khan, S., Hyams, E., Schned, A., Pettus, J. & Halter, R. (2017), 'Comparative study of separation between ex vivo prostatic malignant and benign tissue using electrical impedance spectroscopy and electrical impedance tomography.', *Physiological Measurements* . https://doi.org/10.1088/1361-6579/aa660e.

Park, Y., Reichel, L., Rodriguez, G. & Yu, X. (2018), 'Parameter determination for tikhonov regularization problems in general form.', *Journal of Computational and Applied Mathematics* . https://doi.org/10.1016/j.cam.2018.04.049.

Pasini, A., Lovecchio, J., Cortesi, M., Liverani, C., Spadazzi, C., Mercatali, L., Ibrahim, T. & Giordano, E. (2021), 'Perfusion flow enhances viability and migratory phenotype in 3d-cultured breast cancer cells.', *Annals of Biomedical Engineering* . https://doi.org/10.1007/s10439-021-02727-w.

REFERENCES

Pasini, A., Lovecchio, J., Ferretti, G. & Giordano, E. (2017), 'Medium perfusion flow improves osteogenic commitment of human stromal cells.', *Stem Cells International* . https://doi.org/10.1155/2019/1304194.

Passini, E., Britton, O., Rong Lu, H., Rohrbacher, J., Hermans, A., Gallacher, D., Greig, R., Bueno-Orovio, A. & Rodriguez, B. (2017), 'Human in silico drug trials demonstrate higher accuracy than animal models in predicting clinical pro-arrhythmic cardiotoxicity', *Frontiers in Physiology* . https://doi.org/10.3389/fphys.2017.00668.

Picone, G., Cappadone, C., Pasini, A., Lovecchio, J., Cortesi, M., Farruggia, G., Lombardo, M., Gianoncelli, A., Mancini, L., Menk, R., Donato, S., Giordano, E. & Malucelli E. andd Iotti, S. (2020), 'Analysis of intracellular magnesium and mineral depositions during osteogenic commitment of 3d cultured saos2 cells', *International Journal of Molecular Sciences* . https://doi.org/10.3390/ijms21072368.

Samoré, A., Guermandi, M., Placati, S. & Guerrieri, R. (2017), 'Parametric detection and classification of compact conductivity contrasts with electrical impedance tomography.', *IEEE Transactions on Instrumentation and Measurement* . https://doi.org/10.1109/TIM.2017.2711818.

Shiraz, A., Khodadad, D., Nordebo, S., Yerworth, R., Frerichs, I., van Kaam, A., Kallio, M., Papadouri, T., Bayford, R. & Demosthenous, A. (2019), 'Compressive sensing in electrical impedance tomography for breathing monitoring.', *Physiological Measurements* . https://doi.org/10.1088/1361-6579/ab0daa.

Tan, C., Liu, S., Jia, J. & Dong, F. (2020), 'A wideband electrical impedance tomography system based on sensitive bioimpedance spectrum bandwidth', *IEEE Transactions on Instrumentation and Measurement* **69**, 144–154.

Tikhonov, A. N. & Glasko, V. B. (1965), 'Use of the regularization method in nonlinear problems', *USSR Computational Mathematics and Mathematical Physics* . https://doi.org/10.1016/0041-5553(65)90150-3.

Wu, H., Yang, Y., Bagnaninchi, P. & Jia, J. (2019), 'Calibrated frequency-difference electrical impedance tomography for 3d tissue culture monitoring.', *IEEE Sensors Journal* . https://doi.org/10.1109/JSEN.2019.2919182.

Wu, H., Zhou, W., Yang, Y., Jia, J. & Bagnaninchi, P. (2018), 'Exploring the potential of electrical impedance tomography for tissue engineering applications.', *Materials* . https://doi.org/10.3390/ma11060930.

Yang, Y., Wu, H., Jia, J. & Bagnaninchi, P. (2019), 'Scaffold-based 3-d cell culture imaging using a miniature electrical impedance tomography sensor.', *IEEE Sensors Journal* . https://doi.org/10.1109/JSEN.2019.2924154.